High-efficiency second-harmonic generation in doubly-resonant $\chi^{(2)}$ microring resonators

Zhuan-Fang Bi,[1,2,3] **Alejandro W. Rodriguez,**[2,3,*] **Hila Hashemi,**[3] **David Duchesne,**[4] **Marko Loncar,**[2] **Ke-Ming Wang,**[1,5] **and Steven G. Johnson**[3]

[1]*School of Physics, Shandong University, Jinan, Shandong 250100, China*

[2]*School of Engineering and Applied Sciences, Harvard University, Cambridge, Massachusetts 02138, USA*

[3]*Department of Mathematics, Massachusetts Institute of Technology, Cambridge, Massachusetts 02139, USA*

[4]*Department of Physics, Massachusetts Institute of Technology, Cambridge, Massachusetts 02139, USA*

[5]*State Key Laboratory of Crystal Material, Shandong University, Jinan, Shandong 250100, China*

[*]*alexrod7@mit.edu*

Abstract: By directly simulating Maxwell's equations via the finite-difference time-domain (FDTD) method, we numerically demonstrate the possibility of achieving high-efficiency second harmonic generation (SHG) in a structure consisting of a microscale doubly-resonant ring resonator side-coupled to two adjacent waveguides. We find that $\gtrsim 94\%$ conversion efficiency can be attained at telecom wavelengths, for incident powers in the milliwatts, and for reasonably large bandwidths ($Q \sim 1000$s). We demonstrate that in this high efficiency regime, the system also exhibits limit-cycle or bistable behavior for light incident above a threshold power. Our numerical results agree to within a few percent with the predictions of a simple but rigorous coupled-mode theory framework.

© 2012 Optical Society of America

References and links

1. A. Rodriguez, M. Soljačić, J. D. Joannopulos, and S. G. Johnson, "$\chi^{(2)}$ and $\chi^{(3)}$ harmonic generation at a critical power in inhomogeneous doubly resonant cavities," Opt. Express **15**(12), 7303–7318 (2007).
2. H. Hashemi, A. W. Rodriguez, J. D. Joannopoulos, M. Soljacic, and S. G. Johnson, "Nonlinear harmonic generation and devices in doubly resonant Kerr cavities," Phys. Rev. A **79**(1), 013812 (2009).
3. V. S. Ilchenko, A. A. Savchenkov, A. B. Matsko, and L. Maleki, "Nonlinear Optics and Crystalline Whispering Gallery Mode Cavities," Phys. Rev. Lett. **92**(4), 043903 (2004).
4. J. U. Fürst, D. V. Strekalov, D. Elser, M. Lassen, U. L. Andersen, C. Marquardt, and G. Leuchs, "Naturally Phase-Matched Second-Harmonic Generation in a Whispering-Gallery-Mode Resonator," Phys. Rev. Lett. **104**(15), 153901 (2010).
5. P. S. Kuo and G. S. Solomon, "On- and off-resonance second-harmonic generation in GaAs microdisks," Opt. Express **19**(18), 16898–16918 (2011).
6. Y. Dumeige and P. Feron, "Wispering-gallery-mode analysis of phase-matched doubly resonant second-harmonic generation," Phys. Rev. A **74**, 063804 (2006).
7. G. T. Moore, K. Koch, and E. C. Cheung, "Optical parametric oscillation with intracavity second-harmonic generation," Opt. Commun. **113**, 463 (1995).
8. M. Liscidini and L. A. Andreani, "Highly efficient second-harmonic generation in doubly resonant planar microcavities," Appl. Phys. Lett. **85**, 1883 (2004).

9. L. Fan, H. Ta-Chen, M. Fallahi, J. T. Murray, R. Bedford, Y. Kaneda, J. Hader, A. R. XZakharian, J. Moloney, S. W. Koch, and W. Stolz, "Tunable watt-level blue-green vertical-external-cavity surface-emitting lasers by intracavity frequency doubling," Appl. Phys. Lett **88**, 251117 (2006).

10. P. Scotto, P. Colet, and M. San Miguel, "All-optical image processing with cavity type II second-harmonic generation," Opt. Lett. **28**, 1695 (2003).

11. M. M. Fejer, "Nonlinear optical frequency conversion," Phys. Today **47**, 25–32 (1994).

12. G. McConnell, A. I. Ferguson, and N. Langford, "Cavity-augmented frequency tripling of a continuous wave mode-locked laser," J. Phys. D: Appl. Phys **34**, 2408 (2001).

13. R. G. Smith, "Theory of intracavity optical second-harmonic generation," IEEE J. Quantum Electron. **6**, 215–223 (1970).

14. A. I. Gerguson and M. H. Dunn, "Intracavity second harmonic generation in continuous-wave dye lasers," IEEE J. Quantum Electron. **13**, 751–756 (1977).

15. M. Brieger, H. Busener, A. Hese, F. V. Moers, and A. Renn, "Enhancement of single frequency SHG in a passive ring resonator," Opt. Commun. **38**, 423–426 (1981).

16. S. Pearl, H. Lotem, and Y. Shimony, "Optimization of laser intracavity second-harmonic generation by a linear dispersion element," J. Opt. Soc. Am. B **16**, 1705 (1999).

17. A. V. Balakin, V. A. Bushuev, B. I. Mantsyzov, I. A. Ozheredov, E. V. Petrov, and A. P. Shkurinov, "Enhancement of sum frequency generation near the photonic band edge under the quasiphase matching condition," Phys. Rev. E **63**, 046609 (2001).

18. G. D. Aguanno, M. Centini, M. Scalora, C. Sibilia, M. Bertolotti, M. J. Bloemer, and C. M. Bowden, "Generalized coupled-mode theory for $\chi^{(2)}$ interactions in finite multi-layered structures," J. Opt. Soc. Am. B **19**, 2111–2122 (2002).

19. A. H. Norton and C. M. de Sterke, "Optimal poling of nonlinear photonic crystals for frequency conversion," Opt. Lett. **28**, 188 (2002).

20. G. D. Aguanno, M. Centini, M. Scalora, C. Sibilia, Y. Dumeige, P. Vidavovic, J. A. Levenson, M. J. Bloemer, C. M. Bowden, J. W. Haus, and M. Bertolotti, "Photonic band edge effects in finite structures and applications to $\chi^{(2)}$ interactions," Phys. Rev. E **64**, 016609 (2001).

21. A. R. Cowan and J. F. Young, "Mode matching for second-harmonic generation in photonic crystal waveguides," Phys. Rev. E **65**, 085106 (2002).

22. A. M. Malvezzi, G. Vecchi, M. Patrini, G. Guizzeti, L. C. Andreani, F. Romanato, L. Businaro, E. D. Fabrizio, A. Passaseo, and M. D. Vittorio, "Resonant second-harmonic generation in a GaAs photonic crystal waveguide," Phys. Rev. B **68**, 161306 (2003).

23. R. Paschotta, K. Fiedler, P. Kurz, and J. Mlynek, "Nonlinear mode coupling in doubly resonant frequency doublers," Appl. Phys. Lett. **58**, 117 (1994).

24. V. Berger, "Second-harmonic generation in monolithic cavities," J. Opt. Soc. Am. B **14**, 1351 (1997).

25. I. I. Zootoverkh, K. N. V., and E. G. Lariontsev, "Enhancement of the efficiency of second-harmonic generation in microlaser," Quantum Electron. **30**, 565 (2000).

26. B. Maes, P. Bienstman, and R. Baets, "Modeling second-harmonic generation by use of mode expansion," J. Opt. Soc. Am. B **22**, 1378 (2005).

27. M. Liscidini and L. A. Andreani, "Second-harmonic generation in doubly resonant microcavities with periodic dielectric mirrors," Phys. Rev. E **73**, 016613 (2006).

28. J. A. Armstrong, N. Bloembergen, J. Ducuing, and P. S. Pershan, "Interactions between light waves in a nonlinear dielectric," Phys. Rev. **127**, 1918–1939 (1962).

29. A. Ashkin, G. D. Boyd, and J. M. Dziedzic, "Resonant optical second harmonic generation and mixing," IEEE J. Quantum Electron. **2**, 109–124 (1966).

30. J. Bravo-Abad, A. W. Rodriguez, P. Bermel, S. G. Johnson, J. D. Joannopoulos, and M. Soljačić, "Enhanced nonlinear optics in photonic-crystal nanocavities," Opt. Express **15**(24), 16161–16176 (2007).

31. Z. Yang, P. Chak, A. D. Bristow, H. M. van Driel, R. Iyer, J. S. Aitchison, A. L. Smirl, and J. E. Sipe, "Enhanced second-harmonic generation in AlGaAs microring resonators," Opt. Lett. **32**(7), 826–828 (2007).

32. L. Caspani, D. Duchesne, K. Dolgaleva, S. J. Wagner, M. Ferrera, L. Razzari, A. Pasquazi, M. Peccianti, D. J. Moss, J. S. Aitchison, and R. Morandotti, "Optical frequency conversion in integrated devices," J. Opt. Soc. Am. B **28**(12), A67–A82 (2011).

33. S. Schiller, "Principles and Applications of Optical Monolithic Total-Internal-Reflection Resonators," Ph.D. thesis, Stanford University, Stanford, CA (1993).

34. Y. Dumeige and P. Feron, "Stability and time-domain analysis of the dispersive tristability in microresonators under modal coupling," Phys. Rev. A **84**(4), 043847 (2011).

35. Z. Y. Ou and H. J. Kimble, "Enhanced conversion efficiency for harmonic generation with double resonance," Opt. Lett. **18**, 1053–1055 (1993).

36. M. Tabor, *Chaos and Integrability in Nonlinear Dynamics: An Introduction* (Wiley, 1989).

37. J. S. Levy, M. A. Foster, A. L. Gaeta, and M. Lipson, "Harmonic generation in silicon nitride ring resonators," Opt. Express **19**(12), 11415–11421 (2011).

38. C. Xiong, W. Pernice, K. K. Ryu, C. Schuck, K. Y. Fong, T. Palacios, and H. X. Tang, "Integrated GaN photonic

circuits on silicon (100) for second harmonic generation," Opt. Express **19**(11), 10462–10470 (2011).

39. M. Gandomkar and V. Ahmadi, "Design and analysis of enhanced second harmonic generation in AlGaAs/AlOx microring waveguide," Opt. Express **19**(10), 9408–9418 (2011).

40. G. Nielson, D. Seneviratne, F. Lopez-Royo, P. Rakich, Y. Avrahami, M. Watts, H. Haus, H. Tuller, and G. Barbastathis, "Integrated wavelength-selective optical MEMS switching using ring resonator filters," IEEE Photon. Technol. Lett. **17**(6), 1190–1192 (2005).

41. R. W. Boyd, *Nonlinear Optics* (Academic Press, 1992).

42. M. Fejer, G. Magel, D. Jundt, and R. Byer, "Quasi-phase-matched second harmonic generation: tuning and tolerances," IEEE J. Quant. Electron. **28**(11), 2631–2654 (1992).

43. A. Fiore, V. Berger, E. Rosencher, P. Bravetti, and J. Nagle, "Phase matching using an isotropic nonlinear optical material," Nature **391**, 463–466 (1997).

44. T. Baehr-Jones, M. Hochberg, C. Walker, and A. Scherer, "High-Q ring resonators in thin silicon-on-insulator," Appl. Phys. Lett. **85**(16), 3346–3347 (2004).

45. I. Tomita, M. Asobe, H. Suzuki, J. Yumoto, and Y. Yoshikuni, "Broadband quasi-phase-matched second-harmonic generation in a nonlinear photonic crystal," J. Appl. Phys. **100**(2), 023120 (2006).

46. J. D. Joannopoulos, S. G. Johnson, J. N. Winn, and R. D. Meade, *Photonic Crystals: Molding the Flow of Light*, 2nd ed. (Princeton University Press, 2008). URL http://ab-initio.mit.edu/book.

47. K. Rivoire, S. Buckley, and J. Vuckovic, "Multiply resonant high quality photonic crystal nanocavities," Appl. Phys. Lett. **99**(1), 013114 (2011).

48. K. Rivoire, S. Buckley, and J. Vuckovic, "Multiply resonant photonic crystal nanocavities for nonlinear frequency conversion," Opt. Express **19**(22), 22198–22207 (2011).

49. K. Rivoire, Z. Lin, F. Hatami, and J. Vuckovic, "Sum-frequency generation in doubly resonant GaP photonic crystal nanocavities," Appl. Phys. Lett. **97**(4), 043103 (2010).

50. K. Rivoire, Z. Lin, F. Hatami, W. T. Masselink, and J. Vuckovic, "Second harmonic generation in gallium phosphide photonic crystal nanocavities with ultralow continuous wave pump power," Opt. Express **17**(25), 22609–22615 (2009).

51. K. Rivoire, S. Buckley, F. Hatami, and J. Vuckovic, "Second harmonic generation in GaP photonic crystal waveguides," Appl. Phys. Lett. **98**(26), 263113 (2011).

52. A. F. Oskooi, D. Roundy, M. Ibanescu, P. Bermel, J. D. Joannopoulos, and S. G. Steven, "MEEP: A flexible free-software package for electromagnetic simulations by the FDTD method," Comp. Phys. Commun. **181**, 687–702 (2010).

53. V. A. Mandelshtam and H. S. Taylor, "Harmonic inversion of time signals and its applications," J. Chem. Phys. **107**(17), 6756–6769 (1997). (See erratum).

54. V. A. Mandelshtam and H. S. Taylor, "Erratum: Harmonic inversion of time signals and its applications," J. Chem. Phys. **109**, 4128 (1998).

55. S. G. Johnson and J. D. Joannopoulos, "Block-iterative frequency-domain methods for Maxwell's equations in a planewave basis," Opt. Express **8**(3), 173–190 (2001). URL http://www.opticsexpress.org/abstract.cfm?URI=OPEX-8-3-173.

56. W. Sohler, H. Hu, R. Ricken, V. Quiring, C. Vannahme, H. Herrmann, D. Büchter, S. Reza, W. Grundkötter, S. O. H. Suche, R. Nouroozi, and Y. Min, "Integrated Optical Devices in Lithium Niobate," Opt. Photonics News **19**(1), 24–31 (2008).

57. Q. Xu and M. Lipson, "Carrier-induced optical bistability in Silicon ring resonators," Opt. Lett. **31**(3), 341–343 (2005).

58. R. G. Hunsperger, *Integrated Optics: Theory and Technology* (Springer-Verlag, 2002).

59. C. L. Chen, *Foundations for Guided-Wave Optics* (Wiley, 2006).

60. K. K. Y. Lee, Y. Avniel, and S. G. Johnson, "Rigorous sufficient conditions for index-guided modes in microstructured dielectric waveguides," Opt. Express **16**, 9261–9275 (2008).

61. P. D. Drummond, K. J. McNeil, and D. F. Walls, "Non-equilibrium transitions in sub/second harmonic generation I: Semiclassical theory," Opt. Acta **27**(3), 321–335 (1980).

62. K. Grygiel and P. Szlatchetka, "Chaos in second-harmonic generation of light. The case of a strain of pulses." Opt. Commun. **91**, 241–246 (1992).

63. E. D. Palik, ed., *Handbook of optical constants of solids II* (Academic Press, 1991).

64. M. Ohashi, T. Kondo, and R. Ito, "Determination of quadratic nonlinear optical coefficient of $Al_xGa_{1-x}As$ system by the method of reflected second harmonics," J. Appl. Phys. **74**(1), 596–601 (1993).

65. C. W. Wong, P. T. Rakich, S. G. Johnson, M. Qi, H. I. Smith, E. P. Ippen, L. C. Kimerling, Y. Jeon, G. Barbastathis, and S.-G. Kim, "Strain-tunable silicon photonic band gap microcavities in optical waveguides," Appl. Phys. Lett. **84**, 1242–1245 (2004).

66. D. Dalacu, S. Frederick, P. J. Poole, G. C. Aers, and R. L. Williams, "Postfabrication fine-tuning of photonic crystal microcavities in InAs/InP quantum dot membranes," Appl. Phys. Lett. **87**(15), 151107 (2005).

67. H. Lohmeyer, J. Kalden, K. Sebald, C. Kruse, D. Hommel, and J. Gutowski, "Fine tuning of quantum-dot pillar microcavities by focused ion beam milling," Appl. Phys. Lett. **92**(1), 011116 (2008).

68. J. Pan, Y. Hio, K. Yamanaka, S. Sandhu, L. Scaccabarozzi, R. Timp, M. L. Povinelli, S. Fan, M. M. Fejer, and J. S.

Harris, "Aligning microcavity resonances in silicon photonic-crystal slabs using laser-pumped thermal tuning," Appl. Phys. Lett. **92**(10), 103114 (2008).

1. Introduction

In this paper, we develop concrete designs for ring-resonator devices (depicted schematically in Fig. 1) that achieve compact, high-efficiency second-harmonic generation (SHG: $\omega_1 \rightsquigarrow \omega_2 = 2\omega_1$) by second-order ($\chi^{(2)}$) optical nonlinearities. By employing a combination of abstract coupled-mode theory (CMT) models and full nonlinear Maxwell finite-difference time-domain (FDTD) simulations, we identify key design criteria for achieving low-power high efficiency operation. Our results extend earlier work which established the theoretical parameters of high-efficiency intra-cavity SHG independent of any particular geometry choice [1, 2], and demonstrates the predictive accuracy of CMT when confronted with the complexities of realistic systems. Intra-cavity SHG in ring-resonator geometries is attractive because of the amenability of such geometries to lithographic fabrication in a variety of materials, but we show that special care is required to satisfy both the frequency-matching condition ($\omega_2 = 2\omega_1$) and also the symmetry-induced selection rules (below). Unlike previous designs for SHG in ring resonators, which focused on either large (millimeter) resonators with ultra-small bandwidths [3–5] or on low-power schemes that ignore down-conversion (or depletion) [6], our design focuses on micron (wavelength-scale) resonators with relatively small bandwidths and large ($\gg 1\%$) conversion efficiencies, and fully incorporates competing effects such as bending losses, down-conversion, and instabilities, which become relevant in this regime. Key to our design is the presence of input/output coupling ports based on waveguides with intentional cutoff frequencies, that allow independent control of the input/output coupling lifetimes, and which play a crucial role in establishing the sensitivity, bandwidth, and critical power of the device. To illustrate these design principles, we begin with a 2d example, and then consider a full 3d design involving a AlGaAs resonator on oxide designed for input light at $1.55\,\mu$m, in which we predict $\approx 94\%$ conversion efficiency with a Q of only 1000 (0.1% bandwidth), for an input power of 30 mW. (We expect that much lower powers can be readily achieved with further optimization, or at the expense of bandwidth and/or efficiency.) Although 2d calculations are quicker, we show that some aspects of the design actually simplify in 3d, as more complicated ring and waveguide structures turn out to be required in 2d in order to achieve the required frequency-matching. In 2d, we are able to validate the semi-analytical CMT against nonlinear FDTD simulations that capture the full complexities of the system. Such low-power high conversion efficiencies could find applications in high-frequency sources [7–9], imaging [10], optical storage [11], and other spectroscopic devices [12] that suffer from a lack of coherent lasers at various wavelengths.

SHG has been studied in many different contexts [13–19], most commonly in waveguides [20–22], in the so-called undepleted pump limit in which down-conversion effects are negligible [6, 23–27]. More recently, as devices have become smaller and as these nonlinear processes have become more important for integrated and ultracompact applications, there has been increased interest in designing techniques and/or devices that lower the power requirements and dimensions, as well as increase the efficiency of these systems [28–32]. Microcavities serve as a promising avenue for such applications: when light is confined in a cavity, restricted to small modal volumes V and confined for long times Q, nonlinear effects are enhanced due to the increased field strength and temporal confinement of the interacting modes, leading to significantly lower power requirements [1, 30, 31, 33] in addition to novel dynamical effects [2, 34]. In doubly-resonant cavities, such benefits are obtained both at the pump ω_1 and harmonic ω_2 frequencies, leading to orders of magnitude improvements in efficiency and power requirements [1, 23, 35]. Specifically, SHG in doubly-resonant cavities bears a number of unique
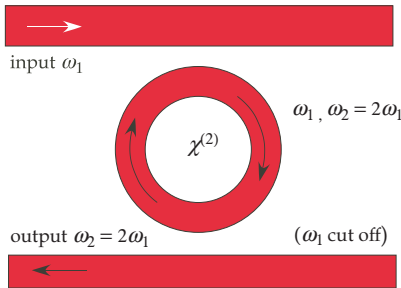
Fig. 1. Schematic ring-resonator waveguide-cavity system: input light from a waveguide supporting a propagating mode of frequency ω_1 (input power $P1, in^2$) is coupled to a ring-resonator cavity mode of frequency ω_1, converted to a cavity mode of twice the frequency $\omega_2 = 2\omega_1$ by a nonlinear $\chi^{(2)}$ process, and coupled out by another waveguide supporting a propagating mode of frequency ω_2 (the waveguide does not support a propagating ω_1 mode).

features [1]: First, there exists a critical power P_{crit}, proportional to V/Q^3, at which 100% efficiency is achieved. For input powers below and above this critical power, the SHG efficiency is significantly reduced. Second, for large powers, the stability of the conversion process is compromised due to bistable behaviors and the system exhibits limit cycles (mathematically known as Hopf bifurcations [36]).

Recently, ring resonator geometries have become an attractive venue for realizing efficient and device-integrated SHG [3–6, 30–32, 37–39]. Ring resonators, like waveguides, offer an advantage over other geometries in that they readily yield modes satisfying the frequency-matching requirement $\omega_2 = 2\omega_1$. To date, however, most works have focused on large (millimeter) ring resonators with long modal lifetimes $Q \gtrsim 10^3$, (and hence narrow bandwidths $1/Q$) in which the long lifetimes (and hence narrow bandwidths $1/Q$) compensate for the relatively large modal volumes [3,4,31,37–39], or on smaller-scale (micron) resonators with more moderate bandwidths ($Q = 10^4$) that operate at low (1%) efficiencies where down-conversion effects can be neglected [5,6], a drawback for applications involving ultracompact integrated devices requiring broad-bandwidth operations, e.g. integrated optical switches [40]. In this paper and unlike previous works, we focus on small (micron-scale) doubly-resonant $\chi^{(2)}$ resonators supporting modes at frequencies ω_1 and $\omega_2 = 2\omega_1$, with moderate lifetimes $Q \sim 1000$s, and at high efficiencies where down-conversion effects cannot be neglected. Here, the significantly smaller Qs are offset by the smaller V, and we find that nearly 100% conversion efficiency is feasible for input powers in the mW range. Our geometry is advantageous in several ways: First, the smaller V translates into more compact operation as well as lower power requirements. Second, in addition to providing a larger bandwidth of conversion, a lower Q also makes the device less sensitive to manufacturing errors—a key consideration since the ring parameters must be carefully chosen to match the frequencies of the fundamental and second-harmonic modes. Third, as noted below, and unlike large-etalon or waveguide setups, the conventional phase matching requirement is replaced by a selection rule on the symmetry of the modes of the resonator that proves significantly simpler to satisfy [41, 42], both experimentally and theoretically. The lack of a phase matching condition is attractive in that it opens up the possibility of studying SHG in materials (e.g. Gallium Arsenide) that are highly nonlinear and practical, but for which phase-matching is difficult because of material dispersion and other issues [43]. A challenging aspect of designing low-power SHG in small ring resonators is the well-known tradeoff between modal volume V and radiation or bending losses (lifetime Q_{rad}) [44]. (Such a tradeoff is absent in complete-gap photonic crystals [1] where SHG has also been considered [45], but

in these systems it seems challenging to procure a design that satisfies the frequency matching condition because of the difficulty of obtaining simultaneous complete gaps at harmonic frequencies in more than one dimension [46]. Recent designs involving PhC nanobeam cavities [47, 48] are promising for both sum-frequency generation [49] and SHG [50, 51].) More importantly, it is well known that side-coupling a waveguide to a small resonator yields additional (and ultimately prohibitive) radiation losses [44], and so we design our geometry to overcome these and other limitations. To aid our design, we employ a CMT formalism that allows us to predict the critical power at which the highest efficiency occurs, and the largest such efficiency, in terms of the lifetimes, modal volumes, and coupling coefficients of the linear modes of the resonator [1]. We supplement this with a full Maxwell simulation via the FDTD method, which incorporates all the complexities of the full system that are neglected by CMT, and we find excellent agreement with CMT.

2. Computational methods

In order to develop the harmonic-generation design, we needed to compute microcavity modes, frequencies, and lifetimes (Q), as well as waveguide dispersion relations. The final design was evaluated both semi-analytically with coupled-mode theory (CMT) and with a full nonlinear Maxwell simulation. We began by studying a two-dimensional (2d) model system, and continued to full 3d calculations. The computational methods for these calculations are described here.

The basic cavity design is that of a ring resonator coupled with one or two adjacent waveguides, as depicted in Fig. 1. To begin with, we studied the isolated cavities, uncoupled to any waveguide. Since the isolated waveguide is axisymmetric, it can be modeled in cylindrical coordinates. We did so using a free finite-difference time-domain (FDTD) software package (Meep) [52]. The simulation cell is surrounded by a perfectly matched layer (PML) absorbing boundary region. The use of cylindrical coordinates in this simulation reduces the 2d problems to a 1d problem, thereby reducing simulation times significantly. Another advantage is that, the angular dependence of the fields in systems with continuous rotational symmetry can be given by the angular momentum parameter (input variable) m, which is easy to control. To begin with, we inserted a broad Gaussian pulse in the structure in order to excite all of the (TM polarized) modes within a chosen bandwidth and with a fixed m; we then re-ran the simulation with a narrow-band source around each mode and outputted the corresponding fields at the end. The resonance frequency and lifetime Q_{rad} were obtained by Harminv, which is a free program to solve the problem of harmonic inversion [53]. The waveguide modes were computed using an iterative eigenmode solver in a planewave basis, using a freely available software package (MPB) [55].

The combined waveguide-cavity system, with waveguides adjacent to the ring resonator, is not axisymmetric and requires a full 2d FDTD calculation. Bringing in the waveguides, there are two decay mechanisms for the modes in this cavity: the mode can decay into the adjacent waveguides, and it can radiate into the surrounding air. The total dimensionless decay rate $1/Q_{tot}$ can be written as the sum of two decay rates: $1/Q_{tot} = 1/Q_w + 1/Q_{rad}$, where $1/Q_w$ and $1/Q_{rad}$ are the waveguide and radiative decay rates, respectively. We obtain Q_{tot} from a filter-diagonalization analysis of the field decay in FDTD [52]. However, we also need to know Q_w and Q_{rad} individually, both of which are modified for different ring–waveguide separations. Therefore, for each separation, we computed the linear transmission spectrum in FDTD. Then, comparing with the transmission equation obtained from coupled mode theory [46],

$$T(\omega) = \frac{P_{out}}{P_{in}} = \frac{\omega_0^2(1/Q_w - 1/Q_{rad})^2 + 4(\omega - \omega_0)^2}{\omega_0^2(1/Q_w + 1/Q_{rad})^2 + 4(\omega - \omega_0)^2},$$ (1)

one can solve for both Q_{rad} and Q_w given $T(\omega_0)$ (the minimum T) and Q_{tot}.

Given the waveguide modes, frequencies, and Q values, the resulting nonlinear system can be modelled semi-analytically using the coupled-mode equations of Ref. [1]. A key parameter of this model is the overlap integral β_1 between the fundamental (ω_1) and harmonic ($\omega_2 = 2\omega_1$) modes, which is computed from the following integral:

$$\beta_1 = \frac{1}{4} \frac{\int d^3\mathbf{x} \sum_{ijk} \varepsilon_0 \chi_{ijk}^{(2)} \left[E_{1i}^*(E_{2j}E_{1k}^* + E_{1j}^*E_{2k}) \right]}{\left(\int d^3\mathbf{x}\,\varepsilon |E_1|^2 \right) \left(\int d^3\mathbf{x}\,\varepsilon |E_2|^2 \right)^{1/2}}, \tag{2}$$

This coupling coefficient can be obtained by applying perturbation theory to Maxwell's equations in the presence of a $\chi^{(2)}$ nonlinearity, as explained in Ref. [1]. Within the CMT, the β_1 coefficient is related to the rate of energy down-conversion. Similarly, there is a corresponding coefficient β_2 that relates to the rate of frequency up-conversion [1]. As shown in [1], these two coefficients are related to one another via conservation of energy: $\omega_1\beta_1 = \omega_2\beta_2^*$.

CMT makes several approximations: it assumes that cavity-waveguide and cavity-radiation coupling is weak (high Q), it neglects nonlinear coupling to modes not at $2\omega_1$ (the rotating-wave approximation), it assumes that the input waveguide couples only to a single direction mode of propagation around the ring (clockwise or counterclockwise), and correspondingly that each ring mode couples out to only a single direction of propagation in the waveguides (despite the fact that we use waveguides that are not identical to the ring structure for reasons described below). To ensure that the full complexities of the nonlinear Maxwell equations in this geometry were accurately captured by the coupled-mode equations, we also performed fully nonlinear FDTD simulations (where the nonlinear constitutive equations are solved by Padé approximants [52]). In particular, we excited the input waveguide with a continuous plane wave of frequency ω_1, and computed the SHG power escaping through the output waveguide at ω_2. The nonlinear FDTD calculations were then checked against the CMT predictions, using the frequencies, decay rates, and β_1 coefficient computed from a set of linear FDTD simulations.

In the absence of losses or reflections, 100% conversion is achieved in the steady state. Including losses [1] (Q_{rad} finite), the critical power can be related to the various model parameters,

$$|P_{crit}|^2 = \frac{\omega_1 Q_1}{2|\beta_1|^2 Q_{w,2}Q_{w,1}^3}, \tag{3}$$

and ends up scaling as V/Q^3 [1]. Hence, one can in principle obtain very low-power efficient harmonic conversion by increasing Q and/or decreasing V (i.e., maximize β) [1]. The efficiency decreases if the power is either too low (in the linear regime) or too high (dominated by down-conversion) compared to $|P_{crit}|^2$.

3. 2D Design

In Ref. [1], we showed, conceptually, that 100% second-harmonic conversion efficiency, in the absence of loss, can be obtained by coupling a single input channel to a single output channel via a cavity with two resonant frequencies, ω_1 and $\omega_2 = 2\omega_1$, that are coupled by a second-order nonlinearity. However, a number of difficulties must be addressed in order to obtain a realistic cavity design that achieves the desired characteristics.

- First, the cavity should be compact and support modes of the requisite frequencies. Generally, in order for them to couple nonlinearly, one must also ensure that the modes of the cavity satisfy certain *selection rules* arising from the presence of any cavity symmetries (exact or approximate), a generalization of the "phase-matching" requirement of earlier works [42, 43].

- Second, the cavity quality factors Q should be carefully controlled, as they affect several tradeoffs:

    - The (fractional) bandwidth of conversion is $1/\max(Q_1, Q_2)$.
    - The critical power is proportional to $1/Q_1^2 Q_2$.
    - The sensitivity to perturbations in the structure is determined by $\min(Q_1, Q_2)$.

    Therefore, it is desirable to have a design in which one can choose Q_1 and Q_2 independently (e.g. to obtain $Q_1 = Q_2$ to minimize power for a given bandwidth).

- Third, the design of the input/output waveguide(s) is critical to ensure that the system supports only a single incoming and a single outgoing wave at both ω_1 and ω_2—additional channels will lower the efficiency (unless they have much larger coupling Q) [46].

Before delving into the details of our design, we briefly summarize our findings. To obtain strongly confined modes at both fundamental and harmonic frequencies, the most attractive candidate cavities seem to be microring cavities and related geometries (whereas mechanisms like photonic bandgaps typically cannot confine light at both ω and 2ω in more than one dimension). However, we find (below) that the basic ring-resonator design must be somewhat modified to obtain a strong coupling (β_1) between the ω and 2ω modes. We chose to operate at total Q's of only a few thousand, which allows our design to cover significant bandwidths (e.g. a 10 Gbit/s telecom channel) and this proved computationally convenient because it required simulations of only a few thousand optical periods. It also means that fabrication errors of up to about 0.1% frequency-mismatch can be tolerated (although some mismatch can be compensated by post-fabrication tuning [5, 42]). As described below, we found that obtaining much smaller Qs by decreasing the ring-waveguide separation is also possible (at the cost of higher critical power), although this is ultimately limited by the increasing radiation losses. For the same ring-waveguide separation, it is well known that higher-frequency modes will have higher Q, so coupling the ring to a single waveguide would yield $Q_2 \gg Q_1$. Thus our design goals above favored *two* waveguides coupled to the ring: one waveguide for the ω_1 input and another for the ω_2 output. The third requirement of a single in/out channels led to an unusual requirement in the waveguide design: the output (ω_2) waveguide was designed to have a *low-frequency cutoff* $> \omega_1$ in order to eliminate its ω_1 guided mode.

As a 2d proof of concept, we considered LiNbO$_3$ (permittivity $\varepsilon = 4.84$) as the nonlinear material. When it is poled in the vertical (z) direction (in the direction of the axis of symmetry), LiNbO$_3$ has a nonlinear susceptibility $\chi_{zzz}^{(2)} \approx 41 \times 10^{-12}$ m/V [41] coupling the E_z field to itself, which means that we can work with purely TM-polarized ($\mathbf{E} \parallel \hat{\mathbf{z}}$) waves. (The use of a diagonal $\chi^{(2)}$ component also simplifies FDTD calculations [52].) Our design is such that no additional quasi-phase-matching is necessary, e.g. we need not resort to schemes like alternatingly poling the LiNbO$_3$ in the $\pm z$ directions to have an oscillating $\chi_{zzz}^{(2)}$ [56] (which requires complicated electrical contacting for the oscillating poling field).

3.1. Ring-resonator design

Previously, achieving efficient SHG in waveguides or Fabry–Perot etalons required techniques to obtain "phase-matching" of the fundamental and harmonic modes [43]. Phase matching is a selection rule arising from the approximate translational symmetry for propagation over long uniform regions, according to which the fundamental and harmonic modes must have the same phase velocities in order to couple efficiently. In microcavities where the fields are confined to within a few wavelengths, such a constraint is instead replaced by selection rules resulting from symmetry considerations, which determine whether the overlap integral in Eq. (2) is

nonzero. In our geometry, involving cylindrically symmetric cavities, the fields can be chosen to have azimuthal dependence $\sim e^{im\phi}$, determined by the conserved angular momentum "quantum number" $m \in \mathbb{Z}$. By simple inspection of Eq. (2) for $\chi_{zzz}^{(2)}$ coupling, this leads to the requirement $m_2 = 2m_1$, where m_1 and m_2 are the corresponding quantum numbers of the fundamental and harmonic modes, respectively. Because m is constrained to integer values, perturbing the cavity parameters does not alter the m of a given mode, so the $m_2 = 2m_1$ condition is easy to satisfy and robust. On the other hand, perturbing the cavity parameters does change the frequencies of the modes at given m values, so the key difficulty is to find modes at a given pair of m's that satisfy $\omega_2 = 2\omega_1$.

For any given geometry and given m, we compute the resonant modes of the linear system by FDTD in cylindrical coordinates, which reduces to a 1d problem in r for a given m. We then compute the modes at m_1 and $2m_1$ for various choices of m_1, and vary the geometry until we find a pair of modes with $\omega_2 = 2\omega_1$. (More precisely, the finite bandwidth means that there is some tolerance $\sim 1/Q$ on the frequency mismatch $\Delta\omega = \omega_2 - 2\omega_1 \lesssim \omega_2/Q$.) We began exploring the simplest possible space of designs: we considered a fixed ring width a and varied the inner radius R, as depicted in the right inset of Fig. 2. However finding modes that satisfy both phase- and frequency-matching requirements for this single-ring design, at chosen index contrast, turned out to be unfeasible. In particular, Fig. 2 shows the frequency mismatch $\Delta\omega$ (units of $2\pi c/a$) corresponding to two phase-matched modes with $m_1 = 15$ and $m_2 = 30$, as a function of the ring radius R. As observed, $\Delta\omega$ is always positive and large $\gtrsim 0.04$ $(2\pi c/a)$ relative to the mode bandwidths ($Q \sim 1000$s) considered here, and we obtained similar results for other values of m_1 and other pairs of modes. We therefore abandoned the single-ring design and instead considered a double-ring structure, depicted schematically in the left inset of Fig. 2. (Note that Ref. [6] considered a set of different double-ring structures for SHG, consisting of either multi-layered stacks in the z direction or adjacent rings, in larger resonator geometries. Similar multilayering designs have been studied in the context of phase-matching in waveguides as well [43].) The reason to consider such a structure is based on the fact that, for the single ring resonator, the $\omega_2 = 2\omega_1$ condition was most nearly matched by a pair of modes where the ω_1 mode has approximately even symmetry through the middle of the waveguide and the ω_2 mode was approximately odd-symmetrical. We therefore expect that an air groove introduced within the resonator will affect the ω_1 mode more than the ω_2 mode (which has a node), thereby allowing us to shift ω_1 into $\omega_2/2$. Furthermore, by introducing the air groove off-center in the resonator, we break the approximate mirror symmetry (that is only slightly broken by the small curvature), and thereby allow the ω_1 mode and ω_2 modes to have a much larger overlap integral. (Exactly even and odd modes would not couple at all, a fact we return to in 3d.) Thus, this structure yields two additional degrees of freedom, the widths of the inner and outer rings, w_1 and w_2 respectively, with which it is possible to shift ω_1 relative to ω_2. After a relatively small search through the design space, we settled on a structure having $w_1 = 0.45a$ and $w_2 = 0.35a$, where a denotes the total width of the double-ring structure including the air groove of width $a - w_1 - w_2 = 0.2a$ (labeled in the left inset of Fig. 2). For this configuration, we find that, for the same azimuthal modes $m_1 = 15$ and $m_2 = 30$ as above, $\Delta\omega$ switches sign as R increases and is zero at $R \approx 4.51a$, as shown by the red line of Fig. 2. Using the field patterns of these modes, we also computed the coupling coefficient β_1, which we found to be $\beta_1 \approx 3.178 \times 10^{-5}$ (in units of $\chi^{(2)}/a^{3/2}$).

As described below, the final ring parameters are slightly perturbed by the presence of the input/output waveguides, so our design procedure was to design the isolated ring, design the coupling waveguides as described below, and then tweak the ring design to restore the $\omega_2 = 2\omega_1$ condition. We obtained a final ring radius of $R = 4.585a$ for frequencies $\omega_1 = 0.277172 \cdot 2\pi c/a$ (vacuum wavelength $3.6a$) and $\omega_2 = 0.554344 \cdot 2\pi c/a$ (vacuum wavelength $1.8a$).
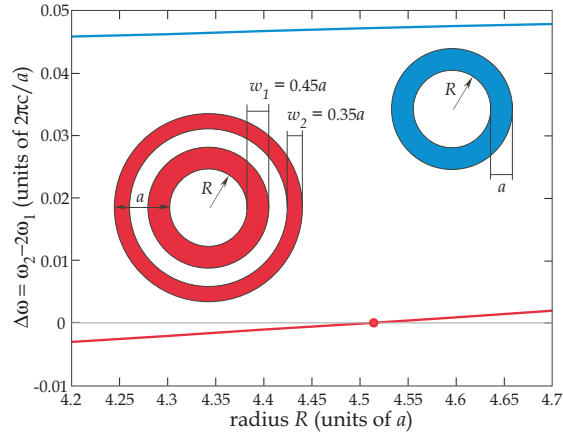
Fig. 2. Plot of the frequency difference $\Delta\omega = \omega_2 - 2\omega_1$ (units of $2\pi c/a$) of two LiNbO$_3$ ring-resonator modes of frequencies ω_1 and ω_2, and azimuthal momentum $m_1 = 15$ and $m_2 = 30$, respectively, corresponding to two different ring-resonator geometries (insets), as a function of inner radius R. The blue and red lines correspond to the single-ring (right inset) and double-ring resonators.

3.2. Input/output coupling waveguides

Given a ring resonator with appropriate modes as described above, we must then design the coupling to adjacent waveguides so that they have the desired coupling lifetimes $Q_{w,1}$ and $Q_{w,2}$ at ω_1 and ω_2. In order to obtain small radiation losses, these coupling lifetimes should be much smaller than the radiative lifetimes $Q_{rad,1}$ and $Q_{rad,2}$ (approximately 10^5 and 10^7 for the isolated ring), the so-called "overcoupled" regime. For this reason, and also to obtain a reasonable bandwidth of conversion, and to limit computation times, we chose to work with $Q_w \sim 10^4$. Furthermore, we don't want to have to bring the waveguide too close to the ring, which would require a high computational resolution and might also induce additional radiative scattering.

In order to obtain Q_w values that are not too large for moderate ring–waveguide separations, we phase-match the waveguide mode to the ring-resonator mode. Conceptually one designs the waveguide to have a phase velocity equal to $m/r\omega$, the phase velocity of the ring mode, but this condition is ambiguous because the "phase velocity" of the ring mode varies with radius r. For a large R, the difference between R and $R + a$ is negligible and so one can simply use a waveguide of the same width as the ring [57]. In our case, however, R/a is too small for this to be a good approximation and an identical waveguide is not optimal. Instead, we varied the waveguide width to minimize Q_w for a given ring–waveguide separation d. Furthermore, this allowed us to have good coupling between the double-ring structure and a simple dielectric waveguide with no air groove, as well as with the cutoff waveguide described below. For example, for the ω_1 mode we found that this procedure corresponded to an optimal phase velocity $m/r\omega$ with $r = R + 1.3a$.

Fixing the waveguide width and varying the ring–waveguide gap d, we obtain the plot of the $Q_{w,1}$ and $Q_{rad,1}$ in Fig. 3(a), which illustrates two effects. First, the coupling Q_w decreases exponentially with d, thanks to the exponentially increasing overlap of the evanescent tails of the waveguide and cavity modes. Second, although for large d the losses Q_{rad} asymptotes to a constant given by the radiation loss of the isolated ring, for sufficiently small d the radiation losses increase due to scattering of the cavity mode from the waveguide. As explained in Sec. 2,
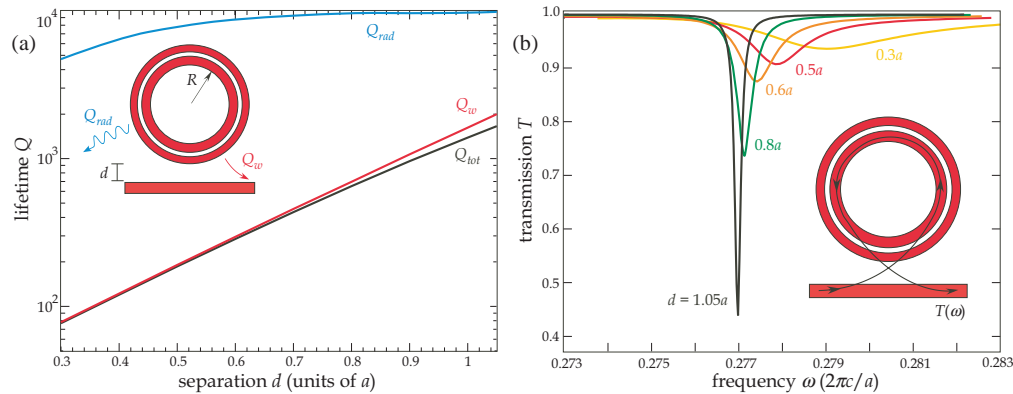
Fig. 3. (a) Semilog plot of the radiative (Q_{rad}), waveguide-coupling (Q_w), and total (Q_{tot}) lifetimes of the ω_1 mode of Fig. 5, as a function of the ring–waveguide separation d_1. (b) Corresponding transmission spectrum at various separations.

we obtain Q_{rad} and Q_w from a combination of mode decay and transmission simulations, and several of these transmission spectra are shown in Fig. 3(b). When $Q_{rad} \gg Q_w$, the linear ring–waveguide system approaches an all-pass filter with 100% transmission (but a resonant delay), while as Q_w approaches Q_{rad} for large d the radiation loss increases and one observes a resonant dip in the transmission.

In principle, we could use a single waveguide to couple ω_1 into the ring resonator and ω_2 out after SHG. However, for the same ring–waveguide separation d the ω_2 mode will normally have $Q_{w,2} \gg Q_{w,1}$ because the evanescent tails of a waveguide mode decay more rapidly at higher frequencies. (Furthermore, if the waveguide is optimized to couple ω_1, the coupling will not be optimized at ω_2.) For example, if we designed the ring to couple to a single dielectric waveguide at ω_1 with a gap $d_1 = 0.5a$, we would obtain $Q_{w,1} = 191$ and $Q_{2,w} = 155,000$, and the difference increases for larger d_1. Instead, therefore, we couple ω_2 out with a *second* waveguide that is optimized to couple at that frequency, on the other side of the ring. This introduces a new problem, however: we must prevent the second waveguide from coupling ω_1, since CMT predicts that the introduction of multiple ω_1 channels will lower the attainable conversion efficiency significantly. We solve this problem by designing the second waveguide to have a *low-frequency cutoff* $> \omega_1$, so that ω_1 cannot couple out via that channel. In 3d below, a low-frequency cutoff is introduced simply by the waveguide substrate [58–60]. In our 2d model system here we obtain a cutoff by the simple expedient of placing the ω_2 waveguide next to a perfect electric conductor (PEC). [A low-index dielectric "substrate" (wall) could have been used in 2d to introduce a cutoff similar to 3d, but PEC is computationally convenient and yields qualitatively the same results—the only purpose of the 2d simulations is to qualitatively explore the design space and validate the theory in preparation for the more realistic 3d design of Sec. 4.]

By this procedure, we obtain an input waveguide of width $0.5a$ and an output waveguide of width $0.35a$ (adjacent to PEC), with dispersion relations shown in Fig. 4. Note the cutoff in the ω_2 mode, as desired. In Fig. 5, we show the field distribution of the two modes in the ring resonator coupled with these two waveguides. Note that the ω_2 mode has negligible leakage into the upper waveguide because the coupling Q in that direction is so much larger. Also, note that each ring mode (propagating counter-clockwise) couples primarily to waveguide modes traveling in the same direction. This is critical in order to mimic the theoretically optimal situation as described in Ref. [1]: ω_1 must enter the resonator from a single channel and exit in a
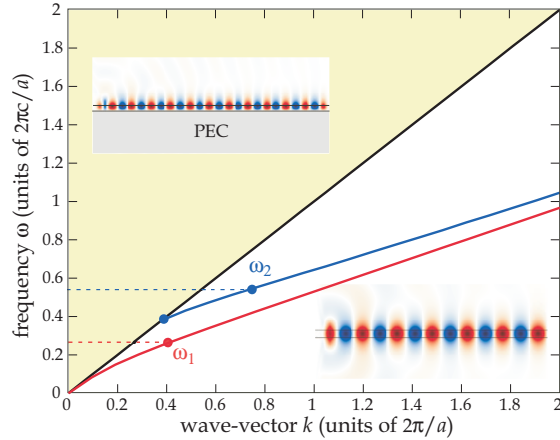
Fig. 4. Band diagram or frequency ω (units of $2\pi c/a$) as a function of wave-vector k (units of $2\pi/a$), corresponding to the fundamental (red line) and second-order (blue line) modes of two different LiNbO$_3$ waveguides of thickness $w_1 = 0.5a$ and $w_2 = 0.35a$, respectively. Here, a denotes the thickness of the double-ring resonator of Fig. 2. The bottom and upper insets show the E_z field profile (blue/white/red denote positive/zero/negative amplitude) of two different modes, with frequencies $\omega_1 = 0.277(2\pi c/a)$ and $\omega_2 = 2\omega_1$, and corresponding wave-vectors $k_1 = 0.39(2\pi/a)$ and $k_2 = 2k_1$, respectively.
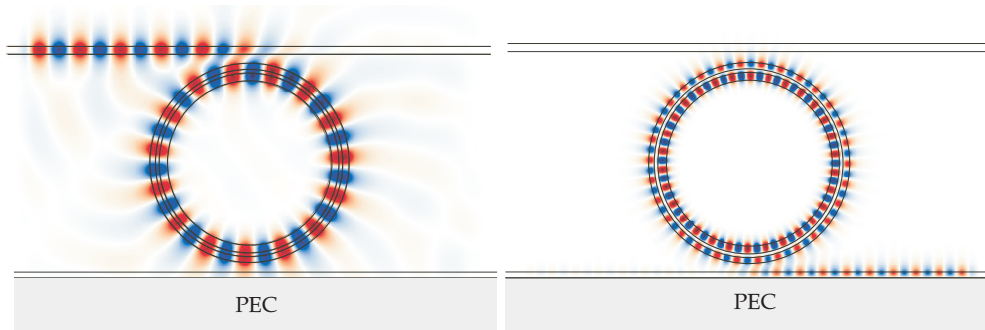
Fig. 5. E_z field snapshot of two double-ring (Fig. 2 inset) resonator modes propagating counter-clockwise, with frequencies $\omega_1 = 0.277(2\pi c/a)$ (left) and $\omega_2 = 2\omega_1$ (right) and azimuthal momentum $m_1 = 15$ and $m_2 = 30$ (effective $k_1 = 0.39(2\pi/a)$ and $k_2 = 2k_1$). The ring resonator is side-coupled to two adjacent waveguides, separated by a distance $d_1 = d_2 = 0.5a$, supporting phase-matched propagating modes at ω_1 (top waveguide) and ω_2 (bottom waveguide).

single channel for ω_1 and in a single channel for ω_2. For the nonlinear simulations below, we use larger values of d_1 and d_2 in order to obtain a lower critical power. In particular, we use $d_1 = 1.05a$ and $d_2 = 0.7a$, obtaining $Q_{w,1} = 2000$ and $Q_{w,2} = 8992$.

3.3. Nonlinear characterization and SHG efficiency

Given these parameters of the linear resonator system, CMT can predict the behavior of the nonlinear system when a $\chi^{(2)}$ is introduced. In particular, it predicts that 82% SHG efficiency should be obtained at a certain critical power ($< 100\%$ because of radiations from the finite Q_{rad}/Q_w). However, as noted in Sec. 2, CMT makes many approximations with respect to the
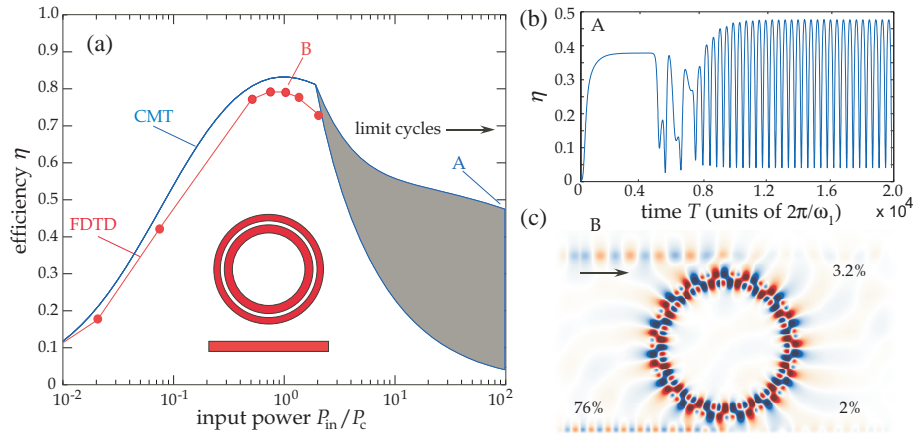
Fig. 6. (a) Plot of SHG efficiency $\eta = P_{SH}/P_{in}$ versus P_{in}, for the double-ring resonator system of Fig. 5 with waveguide-separations $d_1 = 1.05a$ and $d_2 = 0.7a$, obtained both via FDTD simulations (red circles) and CMT (blue line). The gray region denotes the presence of instabilities that lead to limit-cycle behavior. (b) An example of a limit cycle at point A. (c) E_z temporal snapshot of the nonlinear conversion process at point B (the efficiency peak).

full Maxwell equations, and while each of these approximations seems justified in the present case, it is desirable to validate the CMT predictions against a full nonlinear simulation as described in Sec. 2.

In Fig. 6(a), we plot the SHG conversion efficiency (output to the lower waveguide) versus the input power at ω_1, incident from the upper-left port, as computed by both CMT and by nonlinear FDTD (run long enough to reach steady state from zero initial fields). The nonlinear FDTD results agree well with the CMT: the FDTD efficiency peaks at the predicted critical power with a maximum efficiency of 78%, which is reasonable agreement especially considering that it is difficult to determine the resonator Q value from the transmission fits with more than a few percent accuracy. A snapshot of the nonlinear FDTD simulation is shown in Fig. 6(c), in which both the ω_1 input and the ω_2 output are visible (with a complicated superposition of the two modes in the cavity). Most of the 22% of unconverted power is lost to radiation (visible in the plot) due to the finite Q_{rad}/Q_w, but the imperfections represented by these losses also give rise to a few percent of the ω_1 power escaping into the upper-right port and $\approx 2\%$ of the ω_2 power escaping to the lower-right port.

Another intriguing prediction of CMT for intra-cavity SHG is that, once the input power is significantly larger than the critical power, the steady-state solution is replaced by a "self-pulsing" solution in which a constant input power at ω_1 produces an oscillating output power at ω_2 [61]. These "limit cycles" occur in the shaded region of Fig. 6(a), and because the system never reaches a steady state simply taking the efficiency at the end of the simulation gives a somewhat noisy value as seen in this plot from the CMT data. A plot of efficiency vs. time, from the CMT for $P_{in} = 2P_c$, is shown in Fig. 6(b), and the limit cycles are clearly visible (after an initial transient). Note that similar limit cycle (self-pulsing) behaviors in doubly-resonant systems have been theoretically predicted, see e.g. [2, 34, 61, 62]; such limit cycles form a kind of optical oscillator (clock) with a period in the hundreds of GHz or THz (possibly lower depending on the cavity parameters). We have also examined the FDTD behavior in this regime and verified that the FDTD simulations also exhibit limit cycles of the expected period and amplitude.
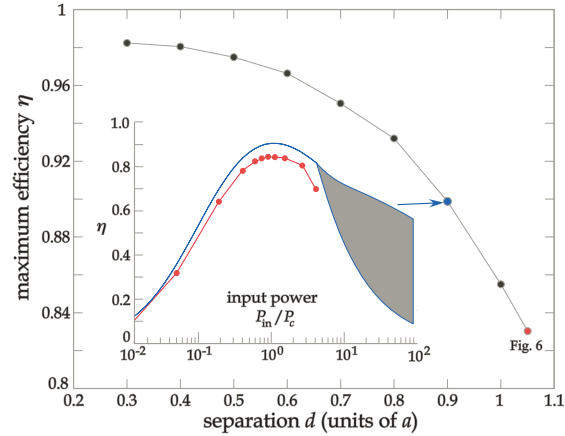
Fig. 7. Maximum efficiency vs. separation distance between input waveguide and ring resonator. (inset: Conversion efficiency from CMT and FDTD in the case $d_1 = 0.9a$)
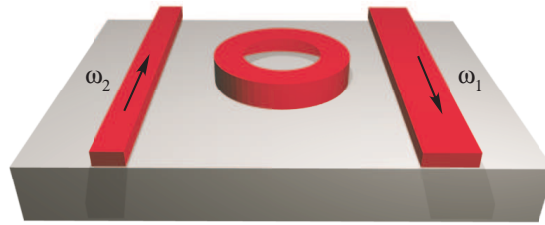

Fig. 8. Schematic diagram of 3d ring-resonator waveguide-cavity system.

When it comes to realistic numbers, we are most interested in the 3d results of the next section, but it is still interesting to estimate the critical power for the 2d system in experimental units, assuming a vacuum wavelength $\lambda_1 = 1.55\,\mu$m for ω_1 (and hence $a = 0.277 \times 1.55 = 0.43\,\mu$m). To obtain a power in W from a 2d calculation, we must assume a certain finite thickness in the z direction, and in this case we assume 200 nm (good vertical confinement), and obtain a critical input power of 800 mW for LiNbO$_3$ at these Q values.

The $< 100\%$ efficiency was due to the finite Q_{rad}/Q_w and in particular the limiting factor is the loss at ω_1 ($Q_{rad,1}/Q_{w,1} = 9847/1998 \approx 4.9$), so we can obtain higher efficiency by making $Q_{w,1}$ smaller. This is accomplished by bringing the input waveguide closer to the ring resonator. Substituting the Q values from Fig. 3 into CMT, we predict an increase in efficiency with decreasing d_1 as shown by the black curve in Fig. 7. The inset of Fig. 7 shows the results in both CMT and FDTD for a separation $d_1 = 0.9a$, for which $Q_{rad}/Q_w = 9616/1043 \approx 9.2$, and obtain 90% and 85% efficiency from CMT and FDTD, respectively.

4. 3D Design

We now apply the same basic principles that we validated in the 2d example to a more realistic 3d design. In 3d, we will consider SHG from $\lambda_1 = 1.55\,\mu$m in a AlGaAs film (aluminum composition $x = 70\%$) bonded to an SiO$_2$ substrate. Note that there are many other possible material choices, e.g. GaAs, GaP and ZnSe. The main criterion for choosing a material is not the usual phase-matching requirement that has driven previous theoretical and experimental works to consider AlGaAs [32], but rather the requirement that the material exhibit relatively

small absorption at these wavelengths. Note also that the choice of 70% Aluminum content is not special; for example, $x = 30\%$ also exhibits relatively low absorption, i.e. $Q_{abs} \gg 10^4$, and yields even larger index contrasts, making the design problem even easier.) As in 2d, we will design a ring resonator to have resonances at ω_1 and $\omega_2 = 2\omega_1$, which is side-coupled to two waveguides for input and output, as shown schematically in Fig. 8. Also as in 2d, we will design the output waveguide to have a low-frequency cutoff $> \omega_1$ so that we can independently control the coupling Q_w for the two frequencies via the respective ring–waveguide gaps. However, there are also several key differences from 2d. First, we include realistic material dispersion of the AlGaAs: its index is 3.023 for ω_1 and 3.178 for ω_2 [63], and these large indices relative to our 2d structure allow a smaller-radius ring for the same Q. AlGaAs has a large *off-diagonal* $\chi^{(2)}$ coefficient ≈ 100 pm/V [5, 6, 41, 64].

For purely off-diagonal components $\chi^{(2)}_{xyz}$, the expression for β_1 in Eq. (2) is slightly more complicated than those involving diagonal $\chi^{(2)}$ components (coupling modes with the same polarization). In this off-diagonal case, it is instructive to explicitly write down the coupling coefficients. Moreover, since our geometry has cylindrical symmetry, it is useful to write down Eq. (2) in cylindrical coordinates. Specifically, if we write the overlap integral in the numerator $\sim 4(E_{1x}E_{1y}E_{2z} + E_{1x}E_{1z}E_{2y} + E_{1y}E_{1z}E_{2x})$ in polar coordinates, using the coordinate transformations $E_x = E_r \cos(\theta) - E_\theta \sin(\theta)$ and $E_y = E_r \sin(\theta) + E_\theta \cos(\theta)$ we find coupling terms of the form:

$$E_{1x}E_{1y} = (E_{1r}^2 - E_{1\theta}^2)\sin(2\theta)/2 + E_{1r}E_{1\theta}\cos(2\theta) \tag{4}$$

$$E_{1x}E_{2y} + E_{2x}E_{1y} = 2(E_{1r}E_{2r} - E_{1\theta}E_{2\theta})\sin(\theta)\cos(\theta)$$
$$+ (E_{1r}E_{2\theta} + E_{2r}E_{1\theta})[\cos^2(\theta) - \sin^2(\theta)]. \tag{5}$$

If we also assume that the fields that are rotationally symmetric functions multiplied by $e^{im_{1,2}\theta}$ (from the rotational symmetry of the ring), and we write $\cos(\theta) = (e^{i\theta} + e^{-i\theta})/2$ and $\sin(\theta) = (e^{i\theta} - e^{-i\theta})/2i$, we obtain an overlap function whose integral in θ is zero unless $m_2 = 2m_1 \pm 2$; this modification to the previous selection rule for a diagonal $\chi^{(2)}$ tensor in section 3, also derived in Ref. [6, 31], results from the additional $e^{\pm i2\theta}$ terms in the integral. Having integrated over θ, we find the following simplified cylindrical overlap integral:

$$\beta_1 = \frac{1}{2}\frac{\int r\,\mathrm{d}r\mathrm{d}z\,\varepsilon_0\chi^{(2)}_{xyz}\left[E_{1r}E_{1\theta}E_{2z} + (E_{1r}E_{2\theta} + E_{2r}E_{1\theta})E_{1z}\right]}{(\int \mathrm{d}^3\mathbf{x}\,\varepsilon|E_1|^2)(\int \mathrm{d}^3\mathbf{x}\,\varepsilon|E_2|^2)^{1/2}}$$
$$\pm \frac{i}{4}\frac{\int r\,\mathrm{d}r\mathrm{d}z\,\varepsilon_0\chi^{(2)}_{xyz}\left[2(E_{1r}E_{2r} - E_{1\theta}E_{2\theta})E_{1z} + (E_{1r}^2 - E_{1\theta}^2)E_{2z}\right]}{(\mathrm{d}^3\mathbf{x}\,\varepsilon|E_1|^2)(\int \mathrm{d}^3\mathbf{x}\,\varepsilon|E_2|^2)^{1/2}}, \tag{6}$$

While the modes in 3d are not purely polarized, because of the near mirror symmetries (both laterally and vertically) for strongly confined modes, in the center of the waveguide they are mostly TE-like (E in-plane) or TM-like (E out-of-plane), and therefore it can be convenient to describe the modes as TE-like or TM-like. (Even for purely symmetric waveguides the modes are only purely polarized in the mid-planes, outside of which they have other components [46]). On the other hand, this terminology can be misleading, because, for example, TM-like modes often have significant in-plane components and hence there can be significant coupling between two TM-like modes. More explicitly, the overlap integral in the numerator of Eq. (6) has nonzero $\sim E_{1\theta}^2 E_{2z}$ terms that couple two TM-like modes (the symmetry allows for a large overlap if E_{2z} is even because $E_{1\theta}$ is squared). (As mentioned in the concluding remarks, preliminary work suggests that the overlap can be significantly improved by optimizing over a wider parameter space to consider additional modes, and at the same time one should obtain
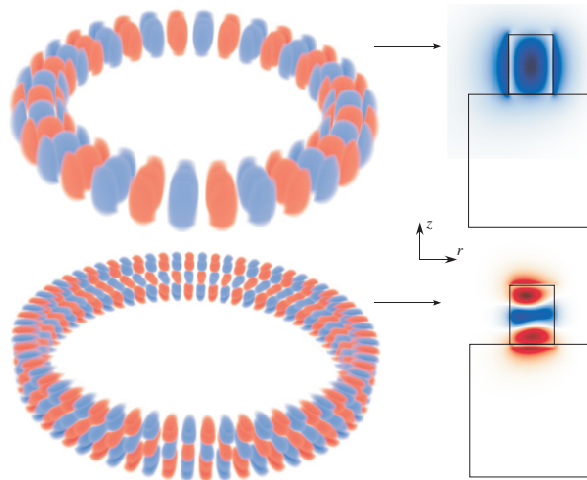
Fig. 9. Field distribution (left) and corresponding lateral cross-section (right) for the (a) ω_1 (E_r component) and (b) ω_2 (E_z component) modes.

modes with higher radiative Q_{rad} to reduce losses.) The ability to couple modes having the same polarization is a dramatic departure from 2d and belies some of the conventional wisdom on this subject.

As a consequence of all of these changes, it turns out that a single ring (no air groove) is sufficient to obtain the desired two modes with both matched frequencies and excellent mode overlap (large β_1). Here, we chose a conventional TE-like to TM-like design that we found by searching through a small space of parameters. We chose a square $a \times 1.35a$ cross-section of the ring waveguide, with an inner radius R and thickness h. The key factor in the ring design is the modified selection rule from the overlap integral of Eq. (6). For several choices of m_1, we varied the ring radius R and looked for $\omega_2 = 2\omega_1$ pairs of modes at each of the two possible m_2 values. We found a suitable pair of modes for $R = 4.6a$, $m_1 = 16$, and $m_2 = 34$, for which $\omega_1 = 0.244 \cdot 2\pi c/a$, corresponding to $a = 0.244 \times 1.55 \, \mu\text{m} = 378$ nm. The resulting field patterns are shown in Fig. 9. As mentioned above, in 3d we use the substrate itself to induce the required low-frequency cutoff, rather than an unphysical perfect metal. We now describe these differences and the resulting 3d design in more detail.

The fields in Fig. 9 are especially attractive because they satisfy a second, *approximate*, selection rule. Because the waveguide width is small compared to the ring radius, the modes closely resemble those of a straight waveguide with the same cross-section, and this cross-section has a mirror symmetry plane bisecting the waveguide perpendicular to the substrate. In a straight waveguide, therefore, all modes would have fields patterns that are either symmetric or anti-symmetric (even or odd) with respect to this mirror. In a ring, the curvature breaks the symmetry but the modes are still *nearly* even or odd with respect to this midplane. In the coupling integral, even or odd ω_1 modes are squared to become even, and hence can only couple to even-symmetry ω_2 modes. Therefore, we should consider only ω_2 modes that have nearly even symmetry such as the one in Fig. 9, as nearly odd ω_2 modes would have nearly zero β_1. As a figure of merit, we can compare the overlap integral β_1 to a "perfect" overlap integral β_0 in which we assume that the fields $= 1$ inside the ring and $= 0$ outside, and we find that $|\beta_1/\beta_0| \approx 0.09$ for our modes, indicating reasonably good overlap. (Better overlaps should be easily achieved.)

For input coupling, we use an $a \times 1.35a$ waveguide identical to the ring cross-section. For
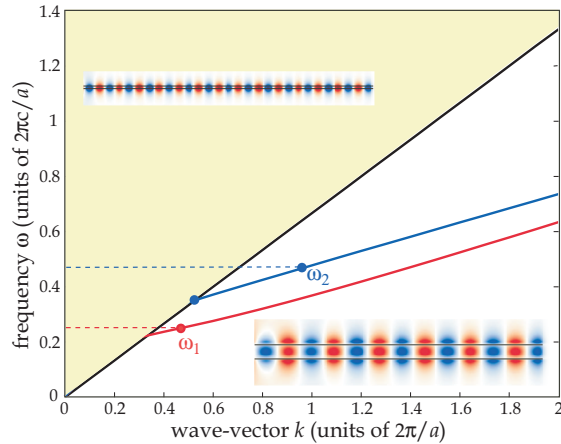
Fig. 10. Band diagram of the 3d waveguides. The bottom and upper insets show the E_r and E_z field profile (blue/white/red denote positive/zero/negative amplitude) of two different modes, with frequencies $\omega_1 = 0.24(2\pi c/a)$ and $\omega_2 = 2\omega_1$, respectively.

output coupling, we reduce the width to $0.14a = 53\,\text{nm}$ so that the waveguide has a low-frequency cutoff $> \omega_1$. The corresponding dispersion relations are shown in Fig. 10. (Note that the substrate causes a cutoff in both waveguides, but the cutoff is $< \omega_1$ for the input waveguide [58–60].)

Since we use separate input/output waveguides, it should be possible to independently control their coupling Q's by varying the waveguide–ring separations. The radiation Q values for the isolated ring are $Q_{rad,1} \approx 1.7 \times 10^4$ and $Q_{rad,2} \approx 10^7$. So, if we choose $Q_{w,1} = 1000$ and $Q_{w,2} = 2000$, CMT predicts a peak of 94% efficiency at a critical power of ≈ 30 mW. As mentioned above, significantly lower critical powers can be easily achieved with further optimization of the structure (larger overlap integrals), and indeed preliminary work suggests the possibility of almost an order of magnitude improvement. Note that as in the 2d example above, and unlike previous work on SHG in GaAs resonator geometries [5, 6] where down-conversion effects were negligible, one can readily observe limit cycle behavior at larger input powers.

5. Concluding remarks

This work demonstrates that a simple two-port, two-mode CMT can accurately capture the complexities involved in a full nonlinear Maxwell system involving rings, losses, and multiple output ports. We have also presented proof-of-concept designs for ring-resonator intra-cavity SHG at high efficiencies and low powers, illustrating the care that is required to obtain appropriate modes and symmetries and in the design of the input/output coupling. However, these designs could be altered in many ways depending upon the needs of a particular experiment. For example, lower powers could be achieved by going to larger Q_w values, at the expense of bandwidth and sensitivity, while increasing the ring radius R in order to prevent radiation loss from increasing. Conversion from $10.6\,\mu$m to $5.3\,\mu$m is especially attractive, both because of the paucity of sources at $5\,\mu$m and also because a $10\times$ increase in lengthscales should simplify fabrication. As can be seen from the comparison of the 2d and 3d designs, the specific parameters of the ring design depend very strongly on the materials (refractive indices and dispersion), the form of the $\chi^{(2)}$ susceptibility, and on the details of the vertical confinement. So, the specific parameter choices here are far from universal, but the basic design principles, especially the selection rules, the role of the different Q values, and the advantage of cutoffs for separate

input/output coupling, will remain.

A key practical concern in any intra-cavity frequency-conversion design such as this one is the sensitivity to fabrication imperfections, which will slightly shift both ω_1 and ω_2. Any overall shift in the frequencies can be compensated by a tunable laser source for the input, in order to match ω_1. However, another tuning parameter is required if imperfections spoil the $\omega_2 = 2\omega_1$ condition. Fortunately, we found in our designs that varying a single parameter, in our case the radius R, was sufficient to bring the frequencies into alignment. Although R cannot easily be changed post-fabrication, other dynamically tunable parameters should play a similar role. For example, strain-induced deformation of the cavity [65] or strain-induced birefringence should affect the ω_1 and ω_2 modes differently and hence be capable of correcting small errors in $\omega_2 - 2\omega_1$. Alternatively, postfabrication wet etching [66] or ion-beam milling [67] can gradually change the geometry for the same purpose. Laser-induced thermal gradients have also been used for postfabrication frequency alignment of cavity frequencies [68].

Acknowledgments